PNAS

Supporting Information for

Curvature gradient drives polarized tissue flow in the Drosophila embryo

Emily W. Gehrels[a,1], Bandan Chakrabortty[a,1], Marc-Eric Perrin[a], Matthias Merkel[b,2], & Thomas Lecuit[a,c,2]

Corresponding authors: Matthias Merkel and Thomas Lecuit

Emails: matthias.merkel@univ-amu.fr; thomas.lecuit@univ-amu.fr

This PDF includes:

Supplementary methods
Supporting Text
Figures S1 to S10
Legends for Movies S1 to S8
SI References

Other supporting materials for this manuscript include the following:

Movies S1 to S8

Supplementary Methods

Fly lines

The following mutant alleles were used: *eve*[3] (Bloomington stock 299), *twi*[1] (Bloomington stock 2381), *sna*[18] (Bloomington stock 2311), *toll*[rm9] and *toll*[rm10] (gift from Maria Leptin), *cta*[RC10] (gift from Maria Leptin), *cic*[1] (gift from Gerardo Jiménez), *traffic jam (tj)-GAL4* (*P{w[+mW.hs]=GawB}NP1624 / CyO, P{w[-]=UAS-lacZ.UW14}UW14*) (Kyoto Stock Center 104055) and *UAS-fat2 RNAi* (*P{GD14442}v27113*) (Vienna Drosophila Resource Center 27113) (gifts from Sally Horne-Badovinac), scabKO (generated in the laboratory using CRISPR by Jean-Marc Philippe), *osk-Gal4*, *UASp-CIBN-pmGFP*, and *UASp-CRY2-RhoGEF2* (gift from Stefano de Renzis). The triple mutant ;*eve*[3], *twist*[1], *snail*[18]; used was generated in the laboratory by Claudio Collinet.

Myosin regulatory light chain (MRLC) is encoded by the gene *spaghetti squash* (*sqh*, Genebank ID: AY122159). Imaging of *sqh* was performed using *sqh-sqh::GFP* (on chromosomes 2 and 3, gift from Robert Karess). Imaging of the plasma membrane was carried out using *sqh-GAP43::mScarlet* (on chromosome 2 (9736, 2R, 53B2) and 3 (9744, 3R, 89E11) made in the laboratory by Jean-Marc Philippe). The recombinants ;*sqh-sqh::GFP,sqh-GAP43::mScarlet;* and *;;sqh-sqh::GFP,sqh-GAP43::mScarlet* were generated in the laboratory. All unique fly lines generated for this study are available from the corresponding authors upon reasonable request.

Crosses for *toll vl*: virgin *;sqh-sqh::GFP,sqh-GAP43::mSc;toll*[rm9]*/TM6C* females were crossed with *;sqh-sqh::GFP,sqh-GAP43::mSc;toll*[rm10]*/TM6C* males. Homozygous offspring were put in a cage.

Crosses for *fat2*: virgin ;*tj-Gal4;sqh-sqh::GFP,sqh-GAP43::mSc* females were crossed with ;*UAS-fat2 RNAi;sqh-sqh::GFP,sqh-GAP43::mSc* males. F1 virgins were crossed with ;*UAS-fat2 RNAi;sqh-sqh::GFP,sqh-GAP43::mSc* males. Resulting progeny were put in a cage.

Two photon image analysis

For both membrane and myosin channels, we used ImageJ software to access images of the sagittal section of the embryo from relevant time points by splitting a corresponding time series movie into individual time frames. For extracting the apical and basal contour of the epithelium, we manually segmented a large number of frames to precisely define the respective apical and basal contours. The separation of the apical contour from the vitelline membrane is a non-trivial segmentation task, we therefore used these initially segmented frames to train a Deep Learning algorithm (namely a U-NET (46)) to do similar segmentation automatically for future movies.

To align the embryos in space**,** an ellipse (**Fig. 1 C** dashed blue ellipse) with direction of the principal axis (dashed blue line) towards the posterior side, was fitted on the apical contour of the epithelium at T_{cell} = 0 min (reference time when cellular front of epithelial cells passes the nucleus). The intersection (indicated

by green star) of the principal axis with the midline (in red) of the epithelium is defined as the "zero (s = 0)" reference of the arc-length coordinate.

For myosin quantification, we developed a python script to identify the segmented apical and basal contours as closed polynomials. These polynomials were then discretized by 100 evenly spaced nodes, such that each apical node has a correspondence to the nearest basal node. For each node, a myosin-mask was defined by a quadrilateral with height approximately 10 pixels (determined by the thickness of the myosin signal) and variable width determined by the distance between the adjacent nodes. Myosin intensity at a given node was calculated by averaging the pixel intensities within the respective mask.

To extract model inputs, we constructed a midline contour by a new set of nodes defined by the average of each pair of respective apical and basal nodes. At each midline node, we computed tissue velocity via particle image velocimetry (PIV, using python library openpiv), total myosin intensity (sum of the myosin intensity at the apical and basal nodes), active-moment (product of the difference in myosin intensity at the apical and basal nodes with the distance of the midline node from either the apical or the basal node) and curvature (spatial derivative of the angle between the adjacent pair of midline edges).

Lightsheet image analysis

To analyze the 3D datasets acquired on the lightsheet microscope, we used the z-stack (with slices along the AP axis of the embryo) to locate the DV axis using the direction of movement of the pole cells during the fast phase and the location of the mesoderm invagination. We then resliced the stack perpendicular to the DV axis and selected the plane that cut through the center of the posterior midgut invagination. In this cut through of the embryo, we detected the time at which the cellularization front passed the nucleus (T_{cell} = 0), and the time at which the first point of myosin expression appeared (FirstMyoTime). We then tracked the pole cell movement in time (as in Fig 1D) to determine the moment at which the pole cells first exhibited fast movement. This frame was used as a proxy for symmetry breaking time (T_{asb} = 0). At T_{asb} = 2, 2.5 and 3 min, we measured the extent of the myosin domain (Myo Length) and the average myosin intensity by tracing a freehand line through the punctate myosin expression in FIJI and extracted the average intensity along this line ($\overline{\mathrm{ApMyoInt}}$). This measurement was performed three time at each of the three time points and the nine measurements were averaged to reduce the effect of noise. To account for the effects of varying imaging brightness, we normalized the average myosin intensity by the average basal myosin intensity at T_{cell} = 5 min ($\overline{\mathrm{BasalMyoInt}}$), giving our final measurement for myosin brightness (Avg Myo Int = $\overline{\mathrm{ApMyoInt}}$ / $\overline{\mathrm{BasalMyoInt}}$).

Supporting Text

1 Derivation of the model equation

In this section we derive the model equation Eq. (3) in the main text that predicts the tangential flow in the embryo. In brief, this equation describes the embryo as an overdamped liquid (**Fig. S3A**,**3B**), which is driven by active tensions at the apical and basal surfaces of the epithelium. We use elements from the theory of active surfaces(1).

1.1 Description of the Drosophila embryo as a time-dependent 1D manifold

For simplicity, we describe the *Drosophila* embryo as a time-dependent 1D manifold $\mathbf{x}(s,T)$ that follows the epithelial midline in a mid-sagittal section of the embryo. For given position s and time T, $\mathbf{x}$ is a position in 2D euclidean space, which corresponds to the mid-saggital section when seen from the embryo's right side (as in **Fig. 1A,B** in the main text). It is parameterized by a scalar s such that the manifold is a loop and runs in clockwise sense with increasing s, such that it successively passes through dorsal, anterior, ventral, and posterior part of the embryo, respectively (as in **Fig. 1C** in the main text).

Based on the manifold $\mathbf{x}(s,T)$, we introduce for given s and T the tangent vector $\mathbf{e}$ and length e, unit normal vector pointing outside $\mathbf{n}$, and local curvature c following standard definitions:

$$\mathbf{e} = \partial_s \mathbf{x}$$

$$e = |\mathbf{e}|$$

$$\mathbf{n} = \frac{1}{e}\boldsymbol{\varepsilon}\cdot\mathbf{e} \qquad \text{S1}$$

$$c = -\frac{1}{e^2}(\partial_s \mathbf{e})\cdot\mathbf{n}$$

Here, the tensor $\boldsymbol{\varepsilon}$ is the generator of counter-clockwise rotations

$$\boldsymbol{\varepsilon} = \begin{pmatrix} 0 & -1 \\ 1 & 0 \end{pmatrix}$$

and $\cdot$ denotes the inner product.

Apical and basal surfaces of the embryo are then, respectively:

$$\mathbf{x}^{\frac{a}{b}}(s,T) \quad = \mathbf{x}(s,T) \pm \frac{h}{2}\mathbf{n}(s,T), \qquad \text{S2}$$

where the superscripts a and b correspond to apical and basal surface, and to the signs $+$ and $-$ on the right-hand side, respectively. The variable h denotes the epithelial height. The corresponding tangential vectors are:

$$\mathbf{e}^{\frac{a}{b}} \quad = \partial_s \mathbf{x}^{\frac{a}{b}} = \left(1 \pm \frac{hc}{2}\right)\mathbf{e}. \qquad \text{S3}$$

In the second step, we inserted Eqs. S2 and used the relation $\partial_s \mathbf{n} = c\mathbf{e}$. Moreover, we ignored spatial variations in epithelial height h here (**Fig. S3C**).

1.2 Force and torque balance

To define the tension $\mathbf{t}$ at some position s of the embryo, we consider an imaginary interface at s that is orthogonal to the manifold $\mathbf{x}(s,T)$. Then, $\mathbf{t}$ is defined as the force that the part of the embryo behind this interface (larger s) exerts on the part of the embryo in front of this interface (smaller s). Note that $\mathbf{t}$ is the total interaction force between these two tissue parts, i.e. it generally contains contributions of both passive and active origin. We denote tangential and normal components of $\mathbf{t}$ by:

$$t = \frac{1}{e}\mathbf{e}\cdot\mathbf{t}$$

$$t_n = \mathbf{n}\cdot\mathbf{t}. \qquad \text{S4}$$

Analogously, we define the moment m at position s as the torque that the portion of the embryo behind the interface at s exerts on the portion of the embryo in front of the interface. The variable m corresponds thereby to the torque component perpendicular to the mid-sagittal plane (from right to left side of the embryo). We do not consider any other torque component in our 1D model here. Like the tension $\mathbf{t}$, also the moment m generally contains contributions of both passive and active origin.

We consider three kinds of external forces that are applied on the embryo: (i) a force density f^a describing friction with the vitelline membrane, which acts tangentially on the apical surface, (ii) a normal force density $-p^a$ acting on the apical surface, which corresponds to the normal force by the vitelline membrane (where the embryo touches the vitelline membrane) or the pressure in the perivitelline space (where the embryo does not touch the vitelline membrane), and (iii) a normal force density p^b that corresponds to the yolk pressure. We ignore here a tangential force on the basal surface by yolk viscosity (see Sec 3.2). Ignoring inertia, force and torque balance in terms of t, t_n, and m are then (appendix A):

$$t' + ct_n = -\left(1+\frac{hc}{2}\right)f^a \qquad \text{(tangential force)} \qquad \text{S5}$$

$$t_n' - ct = -\Delta p + \bar{p}hc \qquad \text{(normal force)} \qquad \text{S6}$$

$$m' - t_n = -\frac{h}{2}\left(1+\frac{hc}{2}\right)f^a \qquad \text{(torque)} \qquad \text{S7}$$

where the prime denotes the arc-length derivative, $q' := (\partial_s q)/e$ for any q, $\Delta p = p^b - p^a$ is the pressure difference across the epithelium and $\bar{p} = (p^a + p^b)/2$ is the average pressure.

To obtain our model equation, Eq. (3) in the main text, force and torque balance need to be complemented by constitutive relations, which link embryonic tensions and moments to deformation, deformation rates,

and active apical and basal tensions. To derive these, we follow a virtual work approach. This allows us to properly take active apical and basal tensions into account.

1.3 Virtual work

We consider virtual displacements $\delta\mathbf{x}(s,T)$ of the embryo from $\mathbf{x}(s,T)$ to $\mathbf{x}'(s,T) = \mathbf{x}(s,T) + \delta\mathbf{x}(s,T)$. These virtual displacements induce virtual mechanical work exerted by active apical and basal tensions δW_{act}, work by externally applied forces and torques δW_{ext}, a change of an effective bending energy δU_{bend}, and dissipated heat δW_{diss}. Without inertia, we have:

$$\delta W_{\mathrm{act}} + \delta W_{\mathrm{ext}} = \delta U_{\mathrm{bend}} + \delta W_{\mathrm{diss}}. \tag{S8}$$

We now derive expressions for each of these contributions.

1.3.1 Mechanical work by active apical and basal tensions, δW_{act}

The mechanical work by active apical and basal tensions is:

$$\delta W_{\mathrm{act}} = -\oint t^a_{act}\frac{\delta e^a}{e^a}\, e^a \mathrm{d}s - \oint t^b_{act}\frac{\delta e^b}{e^b}\, e^b \mathrm{d}s = -\oint t^a_{act}\delta e^a\, \mathrm{d}s - \oint t^b_{act}\delta e^b\, \mathrm{d}s. \tag{S9}$$

Here, t^a_{act} and t^b_{act} are apical and basal active tensions, respectively, $\delta e^a/e^a$ and $\delta e^b/e^b$ are local strain in apical and basal surfaces, and $e^a \mathrm{d}s$ and $e^b \mathrm{d}s$ are infinitesimal apical and basal length elements. From Eqs. S3 follows:

$$\delta e^{a/b} \quad = \left(1 \pm \frac{hc}{2}\right)\delta e \pm \frac{h}{2} e \delta c.$$

Insertion into Eq. S9 yields:

$$\delta W_{\mathrm{act}} = -\oint \left[(t_{act} + c m_{act})\frac{\delta e}{e} + m_{act}\delta c\right] e \mathrm{d}s, \tag{S10}$$

where we introduced (total) active tension t_{act} and active moment m_{act} as:

$$t_{act} = t^a_{act} + t^b_{act} \tag{S11}$$

$$m_{act} = \frac{h}{2}(t^a_{act} - t^b_{act}). \tag{S12}$$

1.3.2 Mechanical work by external forces and torques, δW_{ext}

The external forces introduced in Sec 1.2 exert the following mechanical work on the embryo:

$$\delta W_{\mathrm{ext}} = \oint \left[f^a \delta x^a_t - p^a \delta x^a_n\right] e^a \mathrm{d}s + \oint p^b \delta x^b_n\, e^b \mathrm{d}s, \tag{S13}$$

where $\delta x_t^a := \delta \mathbf{x}^a \cdot \mathbf{e}/e$ and $\delta x_n^{a/b} := \delta \mathbf{x}^{a/b} \cdot \mathbf{n}$ are tangential and normal component of the virtual displacements of apical and basal surface, respectively.

Using local force and torque balance, Eqs. S5–S7, this virtual work can also be expressed in terms of tangential tensions t and moments m only (appendix B):

$$\delta W_{\text{ext}} = \oint \left[(t + cm) \frac{\delta e}{e} + m \delta c \right] e \mathrm{d}s. \tag{S14}$$

1.3.3 Effective bending energy, U_{bend}

With an effective bending rigidity κ, the total effective bending energy of the embryo is

$$U_{\text{bend}} = \oint \frac{1}{2} \kappa c^2 \, e \mathrm{d}s.$$

Its variation as a consequence of the virtual displacements $\delta \mathbf{x}$ is:

$$\delta U_{\text{bend}} = \oint \left[\frac{1}{2} \kappa c^2 \frac{\delta e}{e} + \kappa c \delta c \right] e \mathrm{d}s. \tag{S15}$$

Here, we assumed that the local bending rigidity κ does not change when the tissue is strained.

1.3.4 Dissipated heat, δW_{diss}

In our model, we assume that dissipation *within the embryo* occurs only due to viscous friction in tangential direction:

$$\delta W_{\text{diss}} = \oint \eta u_t \frac{\delta e}{e} \, e \mathrm{d}s. \tag{S16}$$

Here, η is an effective 1D tissue viscosity, and u_t is the tangential strain rate. This tangential strain rate is related to the tangential and normal velocity components v and v_n as(1):

$$u_t = \mathrm{v}' + c \mathrm{v}_n.$$

Fig. S3A,**3B** shows that the contribution by the normal motion is negligible in our case, so:

$$u_t \simeq \mathrm{v}'. \tag{S17}$$

1.4 Constitutive relations

Inserting all contributions, Eqs. S10, S16, S15 and S16 with Eq. S17, into Eq. S8 and comparing the coefficients in front of δc, we obtain:

$$m = \kappa c + m_{act}. \tag{S18}$$

Comparing the coefficients in front of δe, we obtain:

$$t + cm = \frac{1}{2}\kappa c^2 + \eta \mathrm{v}' + t_{act} + cm_{act}.$$

Inserting S18, we find:

$$t = \eta \mathrm{v}' + t_{act} - \frac{1}{2}\kappa c^2. \qquad \text{S19}$$

The last term can be interpreted as an affinity of the tissue for regions with a low curvature to reduce its bending energy.

1.5 Model equation

To obtain our model equation, we combine tangential force balance, Eq. S5, with torque balance, Eq. S7:

$$t' + cm' = -\left(1 + \frac{hc}{2}\right)^2 f^a.$$

Inserting the constitutive relations for t and m, Eqs. S19 and S18, we obtain:

$$\eta \mathrm{v}'' + t'_{act} + cm'_{act} = -\left(1 + \frac{hc}{2}\right)^2 f^a. \qquad \text{S20}$$

Here, we assumed homogeneous tissue viscosity η and bending rigidity κ.

Note that using t_{act} and m_{act} from Eqs. S11 and S12 just as ad-hoc expressions for active tension and active torque in a formalism such as in Ref. (1) can lead to the wrong equation. The deeper reason for this is that the active tension in Ref. (1) corresponds to the virtual work performed by linear strain for constant curvature, which corresponds to $t_{act} + cm_{act}$ (compare Eq. S10), while t_{act} is the virtual work performed by linear strain for *zero* curvature.

We set the external force acting tangentially at the apical surface to be a simple substrate friction with the vitelline membrane:

$$f^a = -\gamma \mathrm{v}.$$

Insertion in Eq. S20 yields:

$$\eta \mathrm{v}'' + t'_{act} + cm'_{act} = \left(1 + \frac{hc}{2}\right)^2 \gamma \mathrm{v}. \qquad \text{S21}$$

The prefactor in front of the substrate friction comes from two effects that add each the same factor of $(1 + hc/2)$. First, the friction force f^a is a force per length, and it acts on the apical surface, which is by a factor of $(1 + hc/2)$ longer than the midline (see also S5). Second, since the friction force acts on the apical surface instead of the midline, it locally exerts a torque on the embryo (see also S7), which enters the tangential force balance when eliminating the normal tension t_n.

In our system, we find that hc is smaller than 1, even though it can reach ≈ 0.4 at the poles (**Fig. S3D**). However, at the poles, the epithelium is often further apart from the eggshell, without any noticeable impact on the flow. For simplicity, we thus absorb the factors $(1 + hc/2)$ on the right

hand side of Eq. S21 into a homogeneous friction coefficient γ. Rearranging the terms, we thus have:

$$\eta \mathrm{v}'' - \gamma \mathrm{v} = -t'_{act} - c m'_{act}. \qquad \text{S22}$$

This is equation (3) in the main text (in **Fig. 5D**). Equation (1) (in **Fig. 3A**) follows from leaving away the last term on the right-hand side in Eq. S22, and equation (2) (**Fig. 4A**) results from including a locally increased friction g.

2 Emergence of polarized flow

To illustrate the fundamental mechanism driving polarized flow in our model (**Fig. 5A-C** in the main text), we focus on the simplified situation where the pressure difference Δp is large enough to prevent any invagination. In other words, the embryo midline follows a time-independent curve $\mathbf{x}_{vm}(s)$ prescribed by the vitelline membrane. If we additionally assume for simplicity that the embryo is incompressible and s is an arc-length coordinate, we have:

$$\mathbf{x}(s,T) = \mathbf{x}_{vm}\big(s + s_e(T)\big).$$

In other words, the configuration of the embryo can be entirely described by the time dependence of $s_e(T)$, which describes how the embryo shifts around within the vitelline membrane. Note that the assumption of incompressibility is restricted to this section only; we assume the embryo to be viscous in the rest of our manuscript (except for section 4.4, where we discuss the case of an elastic behavior).

In this case, the interaction between active moment m_{act} and curvature of the vitelline membrane creates an effective force F_{act} that tends to move the whole epithelium in clockwise direction. To see this, we note that such a force corresponds to a virtual work $\delta W_{\mathrm{act}} = F_{act}\delta s_e$. Since the embryo experiences no strain in tangential direction, the virtual mechanical work by apical and basal tensions, Eq. S10, is:

$$\delta W_{\mathrm{act}} = -\oint m_{act}(s)\delta c(s)\,\mathrm{d}s,$$

where $e = 1$ since s is arc length variable here. Using $\delta c(s) = c_{vm}{}'(s + s_e)\delta s_e$, where c_{vm} is the local curvature corresponding to $\mathbf{x}_{vm}$, we get:

$$\delta W_{\mathrm{act}} = -\delta s_e \oint m_{act}(s) c_{vm}{}'(s + s_e)\,\mathrm{d}s.$$

We thus obtain for F_{act}:

$$F_{act} = -\oint m_{act}(s) c_{vm}{}'(s + s_e)\,\mathrm{d}s.$$

Or, using a partial integration:

$$F_{act} = \oint m'_{act}(s) c_{vm}(s + s_e) \mathrm{d}s. \qquad \text{S23}$$

Note that this corresponds to the integral of the left-hand side of the tangential force balance equation, Eq. S20.

3 Orders of magnitude

3.1 Speed of polarized flow

To compute the speed of the polarized flow, we use the scenario discussed in Sec 2, i.e. the pressure is large enough for the embryo to be entirely in contact with the embryo, and the embryo is incompressible in tangential direction. Moreover, we consider here a sagittal section with lateral width Δz, centered around the mid-sagittal plane.

To obtain a rough order of magnitude for the velocity of the polarized flow, we consider an active moment profile of $m_{act}(s) = m^0_{act}$ for $s \in [s_1, s_2]$, and otherwise $m_{act}(s) = 0$. Then we obtain for the effective force F_{act} driving the polarized flow, using Eq. S23:

$$F_{act} = m^0_{act} \Delta c,$$

where $\Delta c = c_1 - c_2$ with $c_1 := c(s_1 + s_e)$ and $c_2 := c(s_2 + s_e)$. The active moment results in our system from an active tension t^0_{act} that appears apically, and with Eq. S12:

$$F_{act} = t^0_{act} \frac{h \Delta c}{2}.$$

We equate this force with a friction force $F_{ext} = \alpha \Delta z L \bar{v}$ against the vitelline membrane, where L is the total length of the embryo and $\alpha = \gamma / \Delta z$ is the friction coefficient between embryo and vitelline membrane. We thus obtain for the average tangential speed $\bar{v}$:

$$\bar{v} = \frac{t^0_{act}}{\Delta z L \alpha} \frac{h \Delta c}{2}.$$

With $t^0_{act}/\Delta z \sim 30$ pN · µm^{-1} (tension of myosin-enriched cell-cell interface in the embryo ~ 300 pN (2) and cell size ~ 10 µm), $L \approx 10^3$ µm, and $h\Delta c \sim 0.3$ (**Fig. S3D**), and a friction right after cellularization of $\alpha \approx 3$ pN · s · µm^{-3} (3), we obtain

$$\bar{v} \sim 0.1 \text{ µm} \cdot \text{min}^{-1}.$$

This suggests that a curvature-to-active-moment coupling would be sufficient to drive the flow with average speed $\bar{v} \sim 1$ µm · min^{-1} when the friction with the egg shell decreases by around an order of magnitude, consistent with our quantitative fits.

3.2 Effect of yolk viscosity

In our modeling we have neglected the yolk viscosity, because its effect can be neglected as compared to the friction of the embryo with the vitelline membrane. The friction coefficient between embryo and vitelline membrane right after cellularization has been determined to be $\alpha \approx 2 \ldots 3$ pN · s · µm^{-3} (3).

To compare this to the mechanical effect of the yolk viscosity on the embryo, we consider a situation where a velocity difference of $\Delta \mathrm{v}$ between dorsal and ventral part of the embryo create a simple shear flow with shear rate $\Delta \mathrm{v}/H$ in the yolk, where $H \approx 50$ µm is the distance between basal surfaces of dorsal and ventral parts of the embryo. This shear flow leads to a friction force density of $f_Y = \eta_Y \Delta \mathrm{v}/H$, where the yolk viscosity was measured to be $\eta_Y \approx 1$ Pa · s (4). The yolk thus exerts a friction force density of maximally $f_Y/\Delta v \approx 0.02$ pN · s · µm^{-3}. This is two orders of magnitude smaller than the friction forces between embryo and vitelline membrane right after cellularization.

4 Model fitting and prediction

4.1 Retrograde flow

To discuss retrograde flow, we first note that equation (2) in **Fig. 4A** of the main text results from Eq. S22 by neglecting the last term and spatially modulating friction:

$$\eta \mathrm{v}'' - (1 + g\Theta_G)\gamma \mathrm{v} = -t'_{act}, \qquad \text{S24}$$

where

$$\Theta_G(s) = \begin{cases} 1 & \text{if } s \in G \\ 0 & \text{if } s \notin G \end{cases}$$

with G being a small region posterior to the apical myosin patch.

Formally, the existence of retrograde flow and its magnitude follows from integrating Eq. S24 over the whole domain of the embryo:

$$\bar{\mathrm{v}} = -\frac{g\ell_G}{L}\bar{\mathrm{v}}_G. \qquad \text{S25}$$

Here, $\bar{\mathrm{v}}$ is the tangential velocity averaged over the whole epithelium, L is the length of the whole epithelium, ℓ_G is the length of region G, and $\bar{\mathrm{v}}_G$ is the tangential velocity averaged over region G. From Eq. S25 with $g > 0$ follows directly that overall average flow $\bar{\mathrm{v}}$ and $\bar{\mathrm{v}}_G$ have opposite sign, implying retrorade flow within G.This is because frictional force in the high friction ($g > 0$) region must be balanced by frictional force in the other, low friction ($g = 0$) region. Since frictional force is proportional to velocity and total force must sum to zero, this means that if the velocity in the low friction region is positive (clockwise), the velocity in the region of high friction will have to be negative (counterclockwise). Moreover, the absence of localized friction, $g = 0$, implies zero average velocity, $\bar{\mathrm{v}} = 0$.

4.2 Model Fitting

To quantitatively compare equations (1)–(3) in the main text (which follow from Eq. S22) to experimental data, we assumed a linear relation between apical and basal active tension, t_{act}^{a} and t_{act}^{b}, and the respective sqh::GFP signal, I_a and I_b:

$$t_{act}^{a} = f_a I_a$$

$$t_{act}^{b} = f_b I_b.$$

We assume that f_a and f_b can be different, where due to the different cytoskeletal structures apically and basally, we expect $f_a > f_b$. According to Eqs. S11 and S12, we thus have:

$$t_{act} = f_a I_a + f_b I_b$$
$$m_{act} = (f_a I_a - f_b I_b)\frac{h}{2}.$$

Insertion into equation (3) in the main text (i.e. Eq. S22) and division by η yields:

$$\mathrm{v}'' - \frac{1}{l_H^2}\mathrm{v} = -r_a I_a' \left(1 + \frac{ch}{2}\right) - r_b I_b' \left(1 - \frac{ch}{2}\right), \qquad \text{S26}$$

where $l_H = \sqrt{\eta/\gamma}$ is the hydrodynamic length scale, $r_a = f_a/\eta$, and $r_b = f_b/\eta$. The parameters r_a and r_b have units of rates per pixel intensity – they indicate how fast the epithelium contracts per pixel intensity of myosin.

We use Eq. S26 to fit model equation (3), while using the correspondingly modified equations to fit equations (1) and (2) in the main text. In particular, we leave out the terms $\sim hc$ on the right-hand side for equations (1) and (2), and we introduce a localized friction for equation (2).

To fit to experimental data, we first use the measured c, I_a,I_b and h to numerically solve Eq. S26 for v at each time step. For this, we discretize this equation in space with regular lattice spacing $\Delta s = 0.01$ and solve the resulting linear equation in $\mathrm{v}(s)$ in python using a sparse matrix inverter.

To obtain the parameters l_H, r_a, and r_b (and g for equation (2)), we always fitted the theoretical predictions for $\mathrm{v}(s)$ to its respective measured curves $\mathrm{v}(s)$ *at all time points simultaneously* between $T_{asb} = -5 \ldots 8$ min. To this end, we used the python routine curve-fit to minimize the squared distances between theoretical and measured v summed over all positions and times (minimal χ^2 plotted in **Fig. 5I**). In particular, we carried out two kinds of simultaneous fits. First, for many fits, we imposed that all parameter values should be the same at all time points. These corresponds to the blue curves in **Fig. 3C,E**, **4D**,**E**, and **5G**,**H**. Second, for some fits, we allowed l_H to be different for each time point, while we imposed that all other parameters have to be the same value at each time point. This corresponds to the magenta curves in **Fig. 5G**,**H** and all the fit curves in **Fig. S6D-E and Fig. S7B-F**.

4.3 Limitation on compression of apical myosin patch

We realized that our fitting of model equation (3) resulted in a substantial increase of the hydrodynamic length scale of over an order of magnitude around the time of symmetry breaking (**Fig. S6D**). Upon close examination of possible causes for this jump, we first noted that assuming a dominant role of apical myosin during the asymmetric phase, the velocity of polarized flow should scale as $\bar{v} \sim f_a I_a/\gamma = I_a r_a l_H^2$. Second, we noticed a steep decrease in velocity in our velocity fit curves in the region where the apical myosin patch is, around $s \approx 0.03$ (magenta curves in **Fig. 5H**, blue region in **Fig. S6E**). This velocity decrease in the fit curves corresponds to a strong contractile flow, which is created by apical myosin and resisted by tissue viscosity. The corresponding contraction rate is of order $\sim f_a I_a/\eta = I_a r_a$. Taken together, in our χ^2 minimization-based fitting, to keep the contraction of the apical myosin patch close to measured values while keeping large enough $\bar{v}$, the hydrodynamic length scale l_H needs to be large during the asymmetric phase.

To test these ideas, we also examined a model where the contraction rate of the region with the apical myosin patch (the primordium) would be limited. Limiting this contraction rate makes sense, because the primordium undergoes isotropic contraction. Indeed, this region around the apical myosin distribution has increased epithelial height in the asymmetric phase (**Fig. S6F**). There will thus be a limit on how far this part of the tissue will be able to contract until elastic resistance prevents further contraction. In our model, we have not included elasticity, which would require including an additional parameter and defining reference states. To keep the model simple, we have decided to study the consequences of a limited primordium contraction rate in a symmetric region around the peak of apical myosin distribution at $s = 0.03$ (**Fig. S6F**) by substantially increasing viscosity in this primordium region (Eq. 4 in **Fig. 7SA**).

We show results of fits where we locally increased viscosity by a factor of $e = 100$ within the primordium region for which we tested different lengths $0 \leq L_E \leq 0.80$. We find that the contraction rate in the primordium region is indeed decreased (**Fig. S7B**). Moreover, the corresponding increase in hydrodynamic length scale is also much smaller now, from $l_H \approx 0.04$ ($40\ \mu m$) during symmetric flow to maximally $l_H \approx 0.4$ ($400\ \mu m$) during asymmetric flow (**Fig. S7C**). We also find that these results are largely independent of the increase in viscosity as long as $e > 10$ (**Fig. S7E**, **F**). Taken together, taking into account a limited primordium contraction rate, our data can be explained better (smaller χ^2, see **Fig. S7D**) and with a smaller decrease in friction with the eggshell.

4.4 Replacing viscous term by an elastic term

As we argue in the main text, deformation rates in the embryo are on the order of 1/50 min^{-1} (Fig. S3A,B), while elastic stresses are expected to relax on time scales of minutes. However, only anisotropic stresses in the epithelial tangent plane are expected to relax, e.g. by T1 transitions. Meanwhile, for an effectively elastic response of cells to changes in their shape and in the absence of cell divisions and extrusion, the embryo is expected to react elastically to local changes in epithelial area. Because our one-dimensional model does not distinguish between isotropic and anisotropic deformation, we compared our model Eq. 3

in Fig. 5 of the main text, which assumes a viscous response of the tissue to stretch, to a model where we replace this viscous response by an elastic response:

$$E\mathrm{u}'' - \gamma \mathrm{v} = -t'_{act} - cm'_{act} \qquad \text{S27}$$

where E is an effective Young's modulus and $\mathrm{u}(\mathrm{s}_0, \mathrm{t}) = \mathrm{s}(\mathrm{t}) - \mathrm{s}_0$ is the displacement field, where we use as reference state s_0 a time point t_0 during cellularization, and $\mathrm{s}(\mathrm{t})$ is the 1D position of the corresponding material point at any later time $\mathrm{t} > \mathrm{t}_0$. Note that Eq. S27, combined with Eqs. S6, S7, S18, and S19 corresponds to the model of an elastic beam with intrinsic stretch $-t_{act}/E$, intrinsic curvature $-m_{act}/\kappa$, the additional curvature term (second term on the right-hand side of Eq. S27), and specific external forces (e.g. friction against the vitelline membrane and the pressure difference between perivitelline space and yolk).

To quantitatively compare to experimental data, we again assumed a linear relation between apical and basal active tension and the respective sqh::GFP signal (as described in Sec. 4.2), which converts Eq. S27 to the following form

$$\mathrm{v} = \frac{f_a}{\gamma} I'_a \left(1 + \frac{ch}{2}\right) + \frac{f_b}{\gamma} I'_b \left(1 - \frac{ch}{2}\right) + \frac{E}{\gamma} \mathrm{u}'' \qquad \text{S28}$$

The right-hand side of this equation contains three unknown parameters, $\frac{f_a}{\gamma}$, $\frac{f_b}{\gamma}$ and $\frac{E}{\gamma}$. To fit to experimental velocity data $\mathrm{v}(s,t)$, we integrate Eq. S28 using Euler steps $\mathrm{u}(\mathrm{s}_0, \mathrm{t} + \Delta\mathrm{t}) = \mathrm{u}(\mathrm{s}_0, \mathrm{t}) + \mathrm{v}(\mathrm{s}_0 + \mathrm{u}(\mathrm{s}_0, \mathrm{t}), \mathrm{t})\Delta\mathrm{t}$ with a time step of $\Delta\mathrm{t} = 0.5\ \mathrm{min}$, initial condition $\mathrm{u}(\mathrm{s}_0, \mathrm{t}_0) = 0$, and with measured time-dependent fields for c, I_a, and I_b, as well as the measured value for h.

To obtain time-independent parameter values for $\frac{f_a}{\gamma}$, $\frac{f_b}{\gamma}$ and $\frac{E}{\gamma}$, we fitted the theoretical predictions for $\mathrm{v}(s,t)$ to its experimentally measured curves at all time points simultaneously, either without curvature term and only during the symmetric phase, i.e. between $T_{asb} = -4 \ldots 0$ min (red curve in **Fig. S10B**), or with curvature term and during both symmetric and asymmetric phases, i.e. between $T_{asb} = -4 \ldots 8$ min (red curve in **Fig. S10C,D**). We find that the elastic model fits the symmetric phase alone relatively well (red curve in **Fig. S10B**), with a total deviation between theoretical and experimentally measured velocity of $\chi^2 = 48.74\ \mu\mathrm{m}^2\ \mathrm{min}^{-2}$, but still less well than our purely viscous model (Eq. 3 in Fig. 5 of the main text), where $\chi^2 = 38.58\ \mu\mathrm{m}^2\ \mathrm{min}^{-2}$. Note that with neither viscous nor elastic term, i.e. for no resistance of the tissue to tangential deformation, we find $\chi^2 = 57.51\ \mu\mathrm{m}^2\ \mathrm{min}^{-2}$. Compared to the purely elastic and viscous models, this indicates that the viscous term is much more effective in describing the tissue response to tangential deformation. The whole process, i.e. symmetric and asymmetric phase, is not well fit by the elastic model (red curves in **Fig. S10 D**), where $\chi^2 = 2537.57\ \mu\mathrm{m}^2\ \mathrm{min}^{-2}$, whereas the viscous model described the process much better with $\chi^2 = 1200.31\ \mu\mathrm{m}^2\ \mathrm{min}^{-2}$ for time-independent parameter values. The reason for this is the virtual absence of polarized flow in the elastic model (red curves in **Fig. S10 C**). The polarized flow is much smaller, because its amplitude is mainly determined by the apical myosin, whose effect is

determined by the parameter $\frac{f_a}{\gamma}$, which is much smaller in the elastic model ($\frac{f_a}{\gamma} = 0.078\ \mu\mathrm{m}^2\ \mathrm{min}^{-1}$, compared to $\frac{f_a}{\gamma} = 551.14\ 0\mu\mathrm{m}^2\ \mathrm{min}^{-1}$ in the viscous model). The drastic difference in this parameter value results from the fact that in the viscous model viscosity contributes to a slowdown of the symmetric part of the flow, allowing for a larger $\frac{f_a}{\gamma}$ for the same magnitude of the symmetric flow. In other words, if in the elastic model $\frac{f_a}{\gamma}$ was set to a large enough value to drive polarized flow with the observed magnitude, then this would lead to a much too strong symmetric flow arising from the apical myosin. In conclusion, while the elastic model could describe the symmetric phase, it cannot describe the polarized flow, and even the symmetric phase alone is better described by our purely viscous model.

4.5 Simulations using a simplified model

To obtain a better intuition, we simplified the embryo by representing its shape as an ellipse (elliptic contour in **Fig. S5A**,**6A**), discretized by 100 evenly spaced nodes. For these simulations we neglected basal myosin and approximated the distribution of apical myosin by a rectangular function (green patch in **Fig. S5B,6B**) with height I_a^{sim}. To simulate equation (2) in the main text, we moreover approximated the patch of increased friction, Θ_G, by another rectangular function (magenta patch in **Fig. S5B**) that advected with the epithelium. In all simulations, we choose I_a^{sim} to be of the order of experimentally measured apical myosin intensity I_a (as in **Fig. 3B**,**D**) and the values of the physical parameters were chosen from the fit values to the experimental data.

We then simulated discrete time steps $\Delta t = 0.5$ min, where at a given time point T_{sim}, we solved equation (2) or (3) in the main text for velocity using the python solver described in the previous section to obtain the velocity field $\mathrm{v}_{sim}(s)$. To further simplify our simulation, we did not allow for any deformation of the epithelium. We thus advanced the whole epithelium at each time step by the distance $\bar{\mathrm{v}}\Delta t$. This introduced a time dependence in our solution for equation (3), due to a changing offset between curvature $c(s)$ and myosin profile $I_a^{sim}(s)$.

Appendix

A. Force and torque balance

To derive the force and torque balance relations, Eqs. S5–S7, we roughly follow the approach from(1).

We start from noting that in an overdamped system, the total force acting on any piece of the embryo between s_1 and s_2 needs to vanish:

$$0 = \mathbf{t}(s_2) - \mathbf{t}(s_1) + \int_{s_1}^{s_2} \left[f^a \frac{1}{e^a} \mathbf{e}^a - p^a \mathbf{n}^a \right] e^a \mathrm{d}s + \int_{s_1}^{s_2} p^b \mathbf{n}^b \, e^b \mathrm{d}s \qquad \text{A1}$$

Here, the terms on the right hand side are the force exerted by the region of the part of embryo behind s_2, the force exerted by the part of the embryo before s_1, the external force exerted on the apical surface, and the external force exerted on the basal surface.

The derivative of Eq. A1 with respect to $s \equiv s_2$ is:

$$0 = \partial_s \mathbf{t} + f^a \mathbf{e}^a + (p^b e^b - p^a e^a)\mathbf{n} \qquad \text{A2}$$

Using Eqs. S3 and the arc-length derivative, $q' := (\partial_s q)/e$ for any q:

$$0 \quad = \mathbf{t}' + f^a \left(1 + \frac{hc}{2}\right)\frac{1}{e}\mathbf{e} + (\Delta p - \bar{p} hc)\mathbf{n}. \qquad \text{A3}$$

Here, we have defined $\Delta p = p^b - p^a$ and $\bar{p} = (p^a + p^b)/2$. Using $\mathbf{t} = t\mathbf{e}/e + t_n \mathbf{n}$ together with the relations $\mathbf{n}' = c\mathbf{e}/e$ and $(\mathbf{e}/e)' = -c\mathbf{n}$, Eq. A3 becomes:

$$\begin{aligned} 0 \quad &= t' \frac{1}{e}\mathbf{e} - ct\mathbf{n} + {t_n}'\mathbf{n} + ct_n \frac{1}{e}\mathbf{e} \\ &\quad + f^a \left(1 + \frac{hc}{2}\right)\frac{1}{e}\mathbf{e} + (\Delta p - \bar{p} hc)\mathbf{n}. \end{aligned}$$

Tangential and normal force balance, Eqs. S5 and Eq. S6, can now be read off directly from tangential and normal part of this equation.

The total torque acting on the same piece of embryo also needs to vanish:

$$\begin{aligned} 0 \quad &= m(s_2) + \mathbf{x}(s_2) \cdot \boldsymbol{\varepsilon} \cdot \mathbf{t}(s_2) \\ &\quad - m(s_1) - \mathbf{x}(s_1) \cdot \boldsymbol{\varepsilon} \cdot \mathbf{t}(s_1) \\ &\quad + \int_{s_1}^{s_2} \mathbf{x}^a \cdot \boldsymbol{\varepsilon} \cdot \left[f^a \frac{1}{e^a}\mathbf{e}^a - p^a \mathbf{n}^a \right] e^a \mathrm{d}s \\ &\quad + \int_{s_1}^{s_2} \mathbf{x}^b \cdot \boldsymbol{\varepsilon} \cdot p^b \mathbf{n}^b \, e^b \mathrm{d}s \end{aligned}$$

The derivative with respect to $s \equiv s_2$ is:

$$\begin{aligned} 0 \quad &= \partial_s m + \mathbf{e} \cdot \boldsymbol{\varepsilon} \cdot \mathbf{t} + \mathbf{x} \cdot \boldsymbol{\varepsilon} \cdot (\partial_s \mathbf{t}) \\ &\quad + \mathbf{x}^a \cdot \boldsymbol{\varepsilon} \cdot [f^a \mathbf{e} - p^a e^a \mathbf{n}] \\ &\quad + \mathbf{x}^b \cdot \boldsymbol{\varepsilon} \cdot p^b e^b \mathbf{n}. \end{aligned}$$

After using Eqs. S1 and S4 as well as consecutive insertion of Eqs. S2 and A2:

$$0 \quad = \partial_s m - e t_n + \frac{h}{2} f^a \mathbf{n} \cdot \boldsymbol{\varepsilon} \cdot \mathbf{e}^a$$

Insertion of Eq. S3 yields torque balance, Eq. S7:

$$0 = m' - t_n + \frac{h}{2}\left(1 + \frac{hc}{2}\right) f^a.$$

B. Virtual work by external forces and torques

Using force and torque balance, we show here that the expressions in Eqs. S13 and S14 for the virtual work by external forces and torques are equivalent(1). To this end, we start with expression Eq. S14:

$$\delta W_{\text{ext}} = \oint \left[(t + cm) \frac{\delta e}{e} + m\delta c \right] e\mathrm{d}s. \qquad \text{B1}$$

Using

$$\begin{aligned} \delta e &= \frac{1}{e}\mathbf{e} \cdot \partial_s \delta\mathbf{x} \\ \delta c &= -\frac{2c}{e^2}\mathbf{e} \cdot \partial_s \delta\mathbf{x} - \frac{1}{e}\mathbf{n} \cdot \partial_s \left(\frac{1}{e} \partial_s \delta\mathbf{x} \right), \end{aligned}$$

Eq. B1 becomes:

$$\begin{aligned} \delta W_{\text{ext}} &= \oint (t - cm) \frac{1}{e}\mathbf{e} \cdot \partial_s \delta\mathbf{x}\, \mathrm{d}s \\ &\quad -\oint m\mathbf{n} \cdot \partial_s \left(\frac{1}{e} \partial_s \delta\mathbf{x} \right) \mathrm{d}s. \end{aligned}$$

After partial integrations:

$$\begin{aligned} \delta W_{\text{ext}} &= -\oint \left(\partial_s \left[(t - cm) \frac{1}{e}\mathbf{e} \right] \right) \cdot \delta\mathbf{x}\, \mathrm{d}s \\ &\quad -\oint \left(\partial_s \left[\frac{1}{e} \partial_s [m\mathbf{n}] \right] \right) \cdot \delta\mathbf{x}\, \mathrm{d}s. \end{aligned}$$

Here, we carried out one partial integration on the first integral and two consecutive partial integrations on the second integral. Using $\mathbf{n}' = c\mathbf{e}/e$:

$$\delta W_{\text{ext}} = -\oint \left(t \frac{1}{e}\mathbf{e} + m'\mathbf{n} \right)' \cdot \delta\mathbf{x}\, e\mathrm{d}s.$$

Using both $\mathbf{n}' = c\mathbf{e}/e$ and $(\mathbf{e}/e)' = -c\mathbf{n}$:

$$\delta W_{\text{ext}} = -\oint \left(t' \frac{1}{e}\mathbf{e} - ct\mathbf{n} + m''\mathbf{n} + cm' \frac{1}{e}\mathbf{e} \right) \cdot \delta\mathbf{x}\, e\mathrm{d}s. \qquad \text{B2}$$

Combining tangential and normal force balance respectively with torque balance, Eqs. S5–S7, we have:

$$\begin{aligned} t' + cm' &= -\left(1 + \frac{hc}{2} \right)^2 f^a \\ m'' - ct &= -\left[\frac{h}{2} \left(1 + \frac{hc}{2} \right) f^a \right]' - \Delta p + \bar{p} hc. \end{aligned}$$

Insertion in B2 yields:

$$\begin{aligned}\delta W_{\text{ext}} &= \oint \left(1+\frac{hc}{2}\right)^2 f^a \frac{1}{e}\mathbf{e}\cdot\delta\mathbf{x}\, e\mathrm{d}s \\ &+\oint \left(\partial_s\left[\frac{h}{2}\left(1+\frac{hc}{2}\right)f^a\right]\right)\mathbf{n}\cdot\delta\mathbf{x}\,\mathrm{d}s \\ &+\oint (\Delta p-\bar{p}hc)\mathbf{n}\cdot\delta\mathbf{x}\, e\mathrm{d}s.\end{aligned}$$

After partial integration of the second integral:

$$\begin{aligned}\delta W_{\text{ext}} &= \oint \left(1+\frac{hc}{2}\right)^2 f^a \frac{1}{e}\mathbf{e}\cdot\delta\mathbf{x}\, e\mathrm{d}s \\ &-\oint \frac{h}{2}\left(1+\frac{hc}{2}\right)f^a(\mathbf{n}\cdot\delta\mathbf{x})'\, e\mathrm{d}s \\ &+\oint \left(1-\frac{hc}{2}\right)p^b\mathbf{n}\cdot\delta\mathbf{x}\, e\mathrm{d}s \\ &-\oint \left(1+\frac{hc}{2}\right)p^a\mathbf{n}\cdot\delta\mathbf{x}\, e\mathrm{d}s.\end{aligned}$$

Using $(\mathbf{n}\cdot\delta\mathbf{x})' = c(\mathbf{e}/e)\cdot\delta\mathbf{x}+\mathbf{n}\cdot\delta\mathbf{x}'$ and $(\mathbf{e}/e)\cdot\delta\mathbf{n} = -\mathbf{n}\cdot\delta\mathbf{x}'$, as well as $\mathbf{n}\cdot\delta\mathbf{n}=0$, this becomes:

$$\begin{aligned}\delta W_{\text{ext}} &= \oint \left(1+\frac{hc}{2}\right)f^a\frac{1}{e}\mathbf{e}\cdot\left(\delta\mathbf{x}+\frac{h}{2}\delta\mathbf{n}\right)e\mathrm{d}s \\ &+\oint \left(1-\frac{hc}{2}\right)p^b\mathbf{n}\cdot\left(\delta\mathbf{x}-\frac{h}{2}\delta\mathbf{n}\right)e\mathrm{d}s \\ &-\oint \left(1+\frac{hc}{2}\right)p^a\mathbf{n}\cdot\left(\delta\mathbf{x}+\frac{h}{2}\delta\mathbf{n}\right)e\mathrm{d}s.\end{aligned}$$

Using Eqs. S2 and S3, as well as $\mathbf{n}\cdot\delta\mathbf{n}=0$:

$$\begin{aligned}\delta W_{\text{ext}} &= \oint f^a\frac{1}{e^a}\mathbf{e}^a\cdot\delta\mathbf{x}^a\, e^a\mathrm{d}s \\ &+\oint p^b\mathbf{n}\cdot\delta\mathbf{x}^b\, e^b\mathrm{d}s \\ &-\oint p^a\mathbf{n}\cdot\delta\mathbf{x}^a\, e^a\mathrm{d}s.\end{aligned}$$

This is the same expression as in Eq. S13.

Figures S1 to S10:

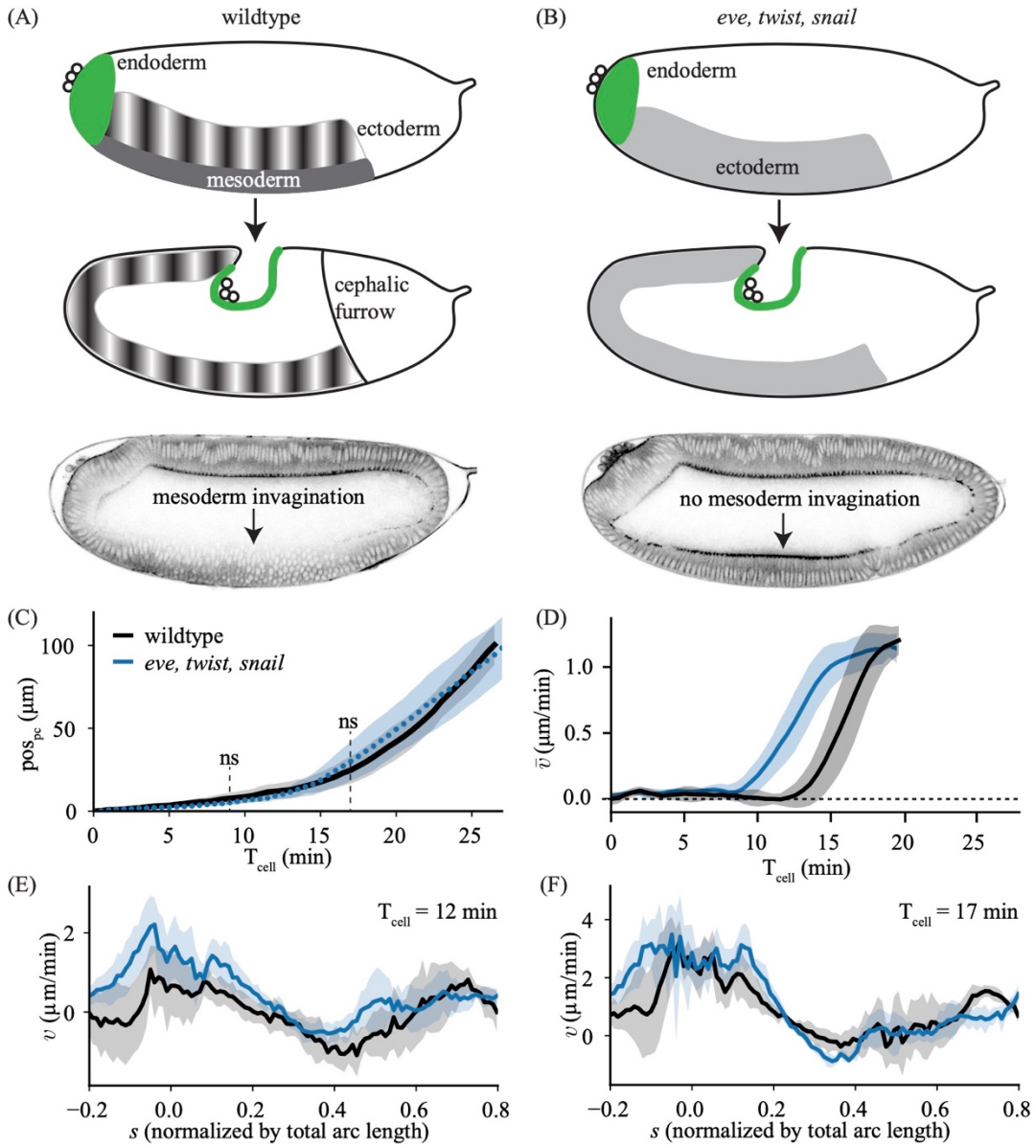

Fig. S1. Comparison of wildtype with *eve, twist, snail* mutant embryos. (A, B) Cartoons of *Drosophila* embryo (*top*) at an early stage, during the process of cellularization and (*middle*) approximately 30 minutes later for a (**A**) wildtype and (**B**) *eve, twist, snail* (*ets*) mutant embryo. This shows that in *ets* mutants the mesoderm is no longer specified, there is no planar polarization of myosin in the ectoderm, and there is no formation of the cephalic furrow. (*bottom*) Images of these embryos at T_{cell} = 19 min. (**C**) Quantification of the position of the pole cells (pos_{pc}) as a function of time since the cellularization front passes the nuclei in the dorsal posterior (T_{cell}). Average performed over 6 wildtype and 7 *ets* embryos. Comparison performed using two-tailed unpaired t-tests. ns, not significant. (**D**) Spatial average of the tangential velocity ($\bar{v}$) as a function of time. Average performed over 5 wildtype and 6 *ets* embryos. (**E, F**) Spatial profile of tangential

velocity for wildtype and *ets* embryos at (**E**) T_{cell} = 12 min and (**F**) T_{cell} = 17 min. Error bars represent standard deviation.

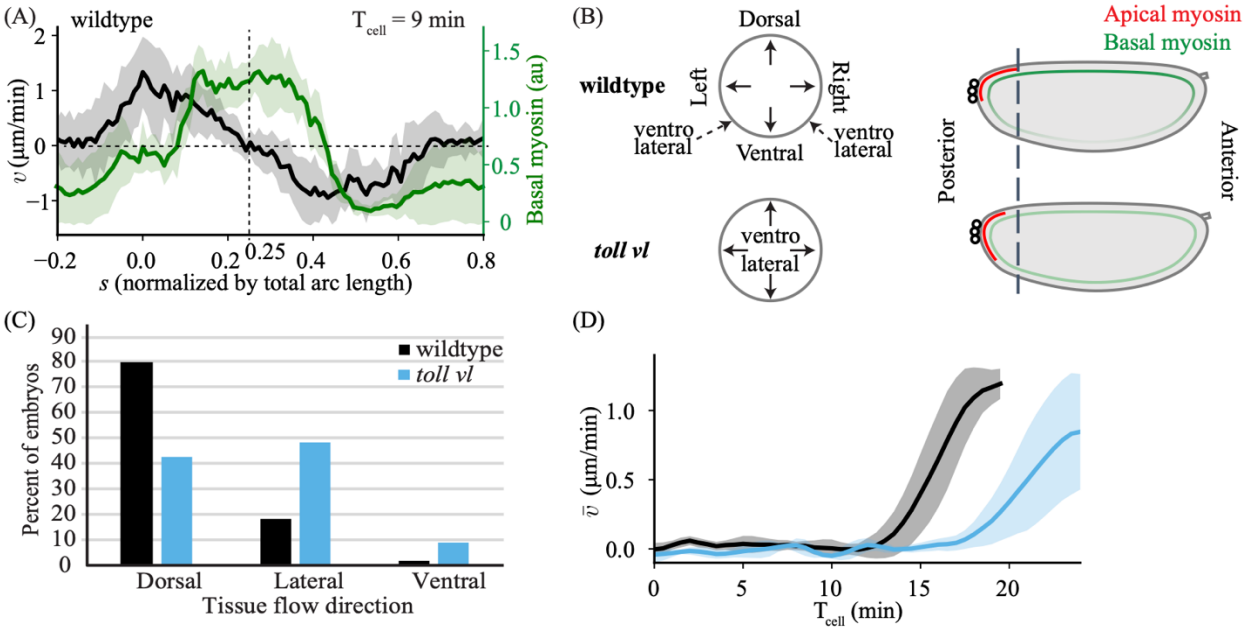

Fig. S2. Characterization of *toll vl* embryos. (**A**) Spatial profile of tangential velocity (v) and basal myosin intensity for wildtype embryos at T_{cell} = 9 min. Vertical dashed line represents the center of the dorsal side of the embryo (s = 0.25). (**B**) Schema of the difference between wildtype and *toll vl* mutant embryos shown in (*left*) a cross section along the anterior-posterior axis and (*right*) in a sagittal plane. (**C**) Quantification of the direction of tissue flow in wildtype and *toll vl* mutant embryos. Dorsal and ventral indicate that the tissue flows in the imaging plane either towards the dorsal or ventral side and lateral refers to any embryo where the tissue flow occurred out of plan. See **Movie S4** for examples of each. Data was collected on a DIC microscope for 58 wildtype embryos and 68 *toll vl* mutant embryos (see **Materials and Methods**). A Fisher's exact test revealed that the distribution of dorsal vs non-dorsal flow outcomes was significantly different between wildtype and *toll vl* conditions ($p < 0.0001$). (**D**) Spatial average of the tangential velocity ($\bar{v}$) as a function of time for wildtype and *toll vl* embryos as in **Fig. 2E**, but including later times. Error bars represent the standard deviation.

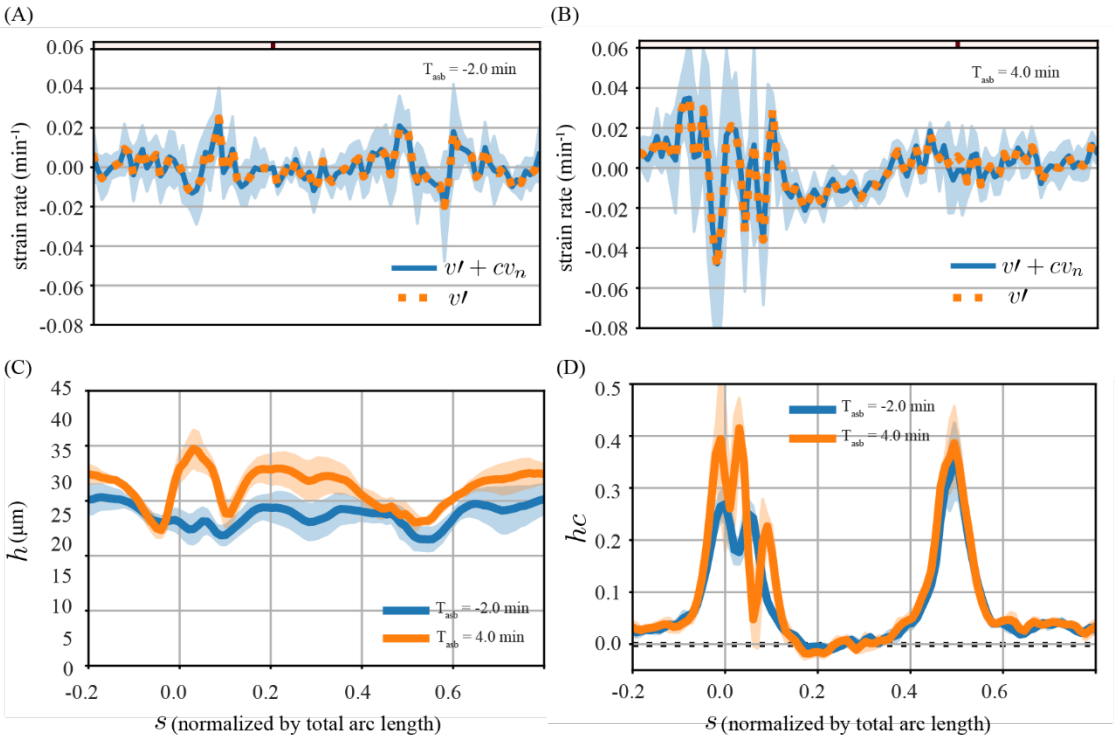

Fig. S3. Orders of magnitude in the experimental data. Data from *eve, twist, snail* mutants, which behave similar to wildtype at early times, but which does not show mesoderm invagination, so the height *h* can be measured more accurately. **(A,B)** The local strain rate (blue solid curve) is virtually identical with the derivative of the tangential velocity v' (orange dashed curve) both at **(A)** T_{asb} = -2 min and **(B)** T_{asb} = 4 min. Bars at top of **A** and **B** show results of two-tailed Student's t-test indicates (white regions – not significantly different, red regions – significantly different with $p < 0.05$). This indicates that the contribution by the normal motion of the epithelium is negligible. **(C)** The fluctuations in epithelial height (*h*) are on the order of 10% (spatial coefficient of variation, $cv \approx 7\%$ at T_{asb} = -2 min and $cv \approx 10\%$ at T_{asb} = 4 min). **(D)** The product *hc* is larger at the poles of the embryo, where it maximally becomes approximately 0.4. In all panels, the shaded regions indicate the standard error of the mean, computed over 6 embryos.

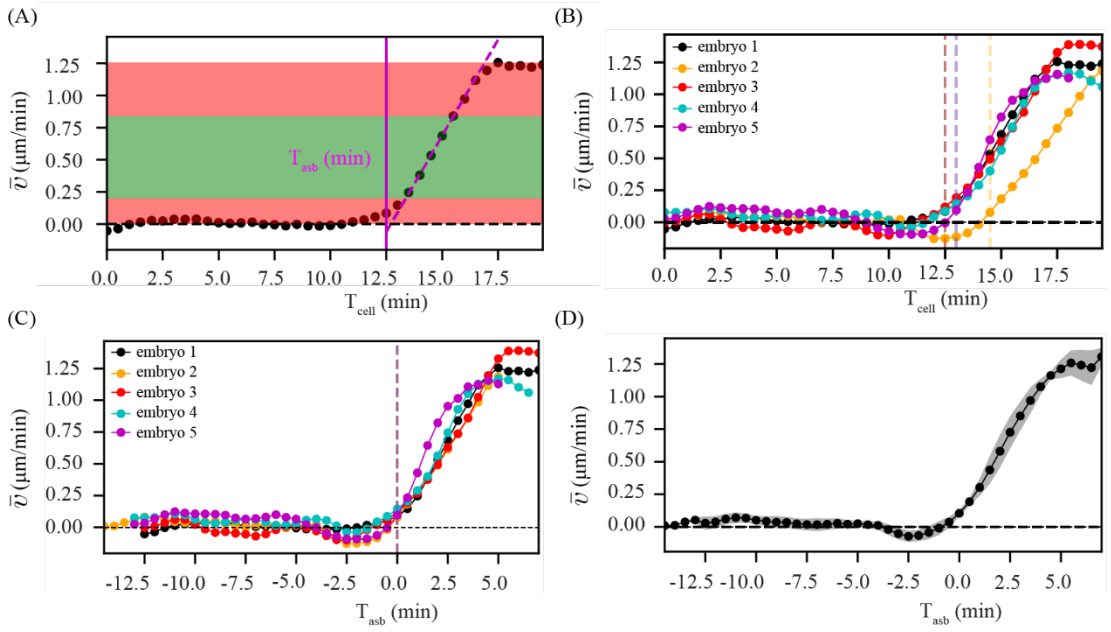

Fig. S4. Detection of symmetric to polarized transition in flow. (A) Temporal profile of the spatially averaged velocity $\bar{v}$ (black dotted curve) computed from the velocity field of individual time frames. A line is fitted in the green region ($\bar{v}$> 0.2 µm/min and the next five time points) to get an intercept with the time axis (T_{cell}). This time of intercept becomes the time of symmetry breaking T_{asb} = 0 (vertical magenta line) and used to align different embryos. **(B)** Temporal profile of $\bar{v}$ with detection of T_{asb} for many embryos, using the method described in **A**. **(C)** Temporal profile of $\bar{v}$ with rescaled time axis, where T_{asb} of the respective embryos is defined as zero reference, i.e T_{asb} < 0 min correspond to symmetric phase of flow and T_{asb} > 0 corresponds to polarized phase of flow. **(D)** Temporal profile of $\bar{v}$, now averaged over all the embryos shown in **C**. The shaded region indicates the standard deviation, computed over 5 embryos.

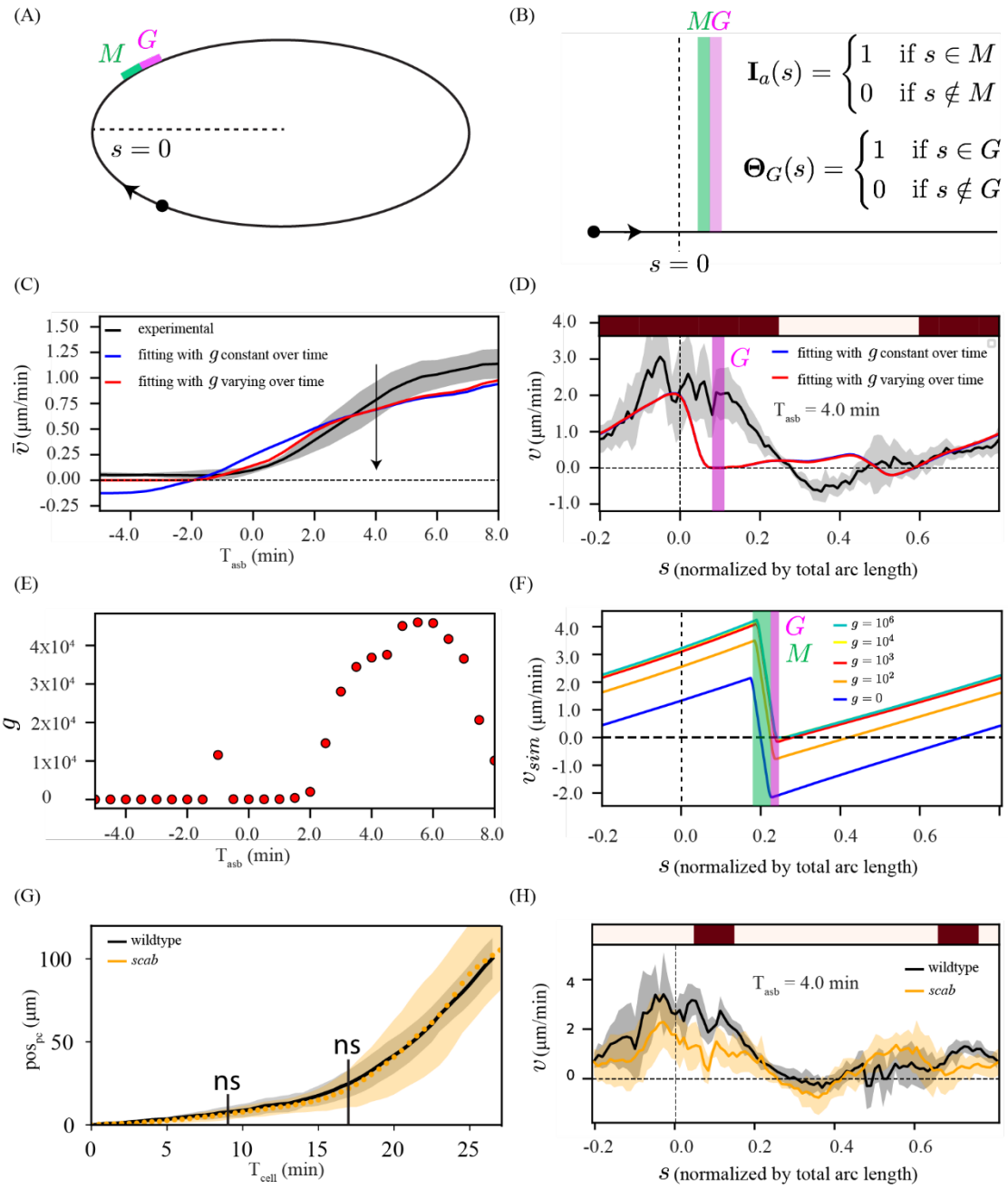

Fig. S5. Fitting with heterogeneous friction. (A) Schematic of the elliptic representation of the embryo. Green region corresponds to domain of myosin (M) and magenta region corresponds to domain of high friction (G). **(B)** 1D flat representation of **A**, where the domains M and G are mathematically described by rectangular functions. **(C)** Experimentally measured temporal profile of spatially averaged velocity $\bar{v}$ (black) and result of two fits (using the procedure described in **Fig. 3**) of equation (2): (blue) all parameters constant and (red) all parameters but *g* constant over time. **(D)** Spatial fit curves for velocity (v), corresponding to the fits in panel **C** for a representative time point during the polarized phase (T_{asb} **=** 4 min). Bar on top indicates results of a single-tailed Student's t-test on the experimental velocity profile (red regions –

significantly greater than zero with p<0.05, white regions – not significantly greater than zero) at the position of high friction. This contradicts the model prediction at this high friction domain. **(E)** Temporal profile of *g* corresponding to the red curves in panel **C** and **D**. **(F)** Elliptic model simulation: spatial profile of velocity (v_{sim}) by simulating equation (2) when myosin intensity (I^a_{sim}) is constant over time, shown for five different values of *g*. These simulations indicate retrograde (counterclockwise) flow in the region of high friction *G*. (**G**) Quantification of the pole cell position (pos_{pc}, see **Materials and Methods**) as a function of T_{cell}. Average performed over 6 wildtype (black) and 6 *scab* (orange) embryos. Comparison shows result of two-tailed unpaired t-tests. ns, sot significant. (**H**) Experimentally measured spatial velocity profile (v) in wildtype (black) and *scab* embryos (orange) at a representative time point T_{asb} = 4 min. Bar on top indicates results of a double-tailed Student's t-test (white regions – not significantly different, red regions – significantly different with p<0.05) at the position of high friction. This contradicts the model prediction at this high friction domain. Average performed over 5 wildtype and 5 *scab* embryos. The shaded regions associated to experimental data is the standard deviation.

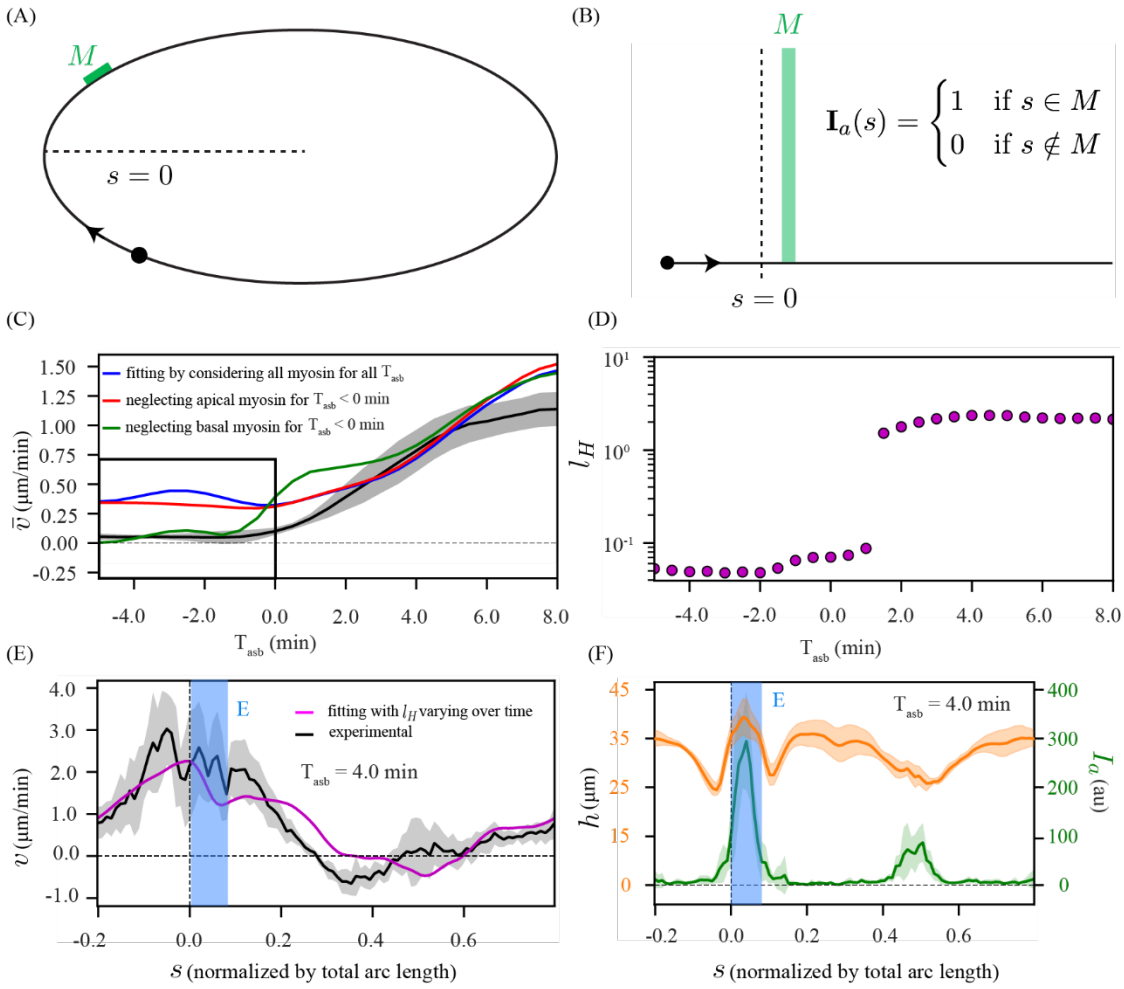

Fig. S6. Fitting with curvature-active moment coupling. (A) Schematic of the elliptic representation of the embryo. Green region corresponds to myosin domain (*M*). **(B)** 1D flat representation of **A**, where the domain M is mathematically described by a rectangular function. **(C)** Experimentally measured temporal profile of spatially averaged velocity $\bar{v}$ (black) and result of three fits (using procedure described in **Fig. 3** in the main text) of equation (3): (1) considering both apical and basal myosin for the entire time range T_{asb} > -5 min (blue), (2) neglecting apical myosin for T_{asb} < 0 min (red) and (3) neglecting basal myosin for T_{asb} < 0 min (green). In fitting all parameters were constant over time. **(D)** Temporal profile of the hydrodynamic length (l_H) corresponding to the magenta curves in **Fig. 5G, H** in the main text. In this plot l_H is given in units of epithelial length L=1000 μm. **(E)** Experimentally measured spatial profile of velocity v (black) and the associated fit curve shown in **Fig. 5H** (magenta, in main text). **(F)** Experimentally measured spatial profile of the epithelial height (h, orange) and apical myosin intensity (I_a, green) at the same time point as in **E**. The shaded regions associated to experimental data is the standard deviation, computed over 6 embryos.

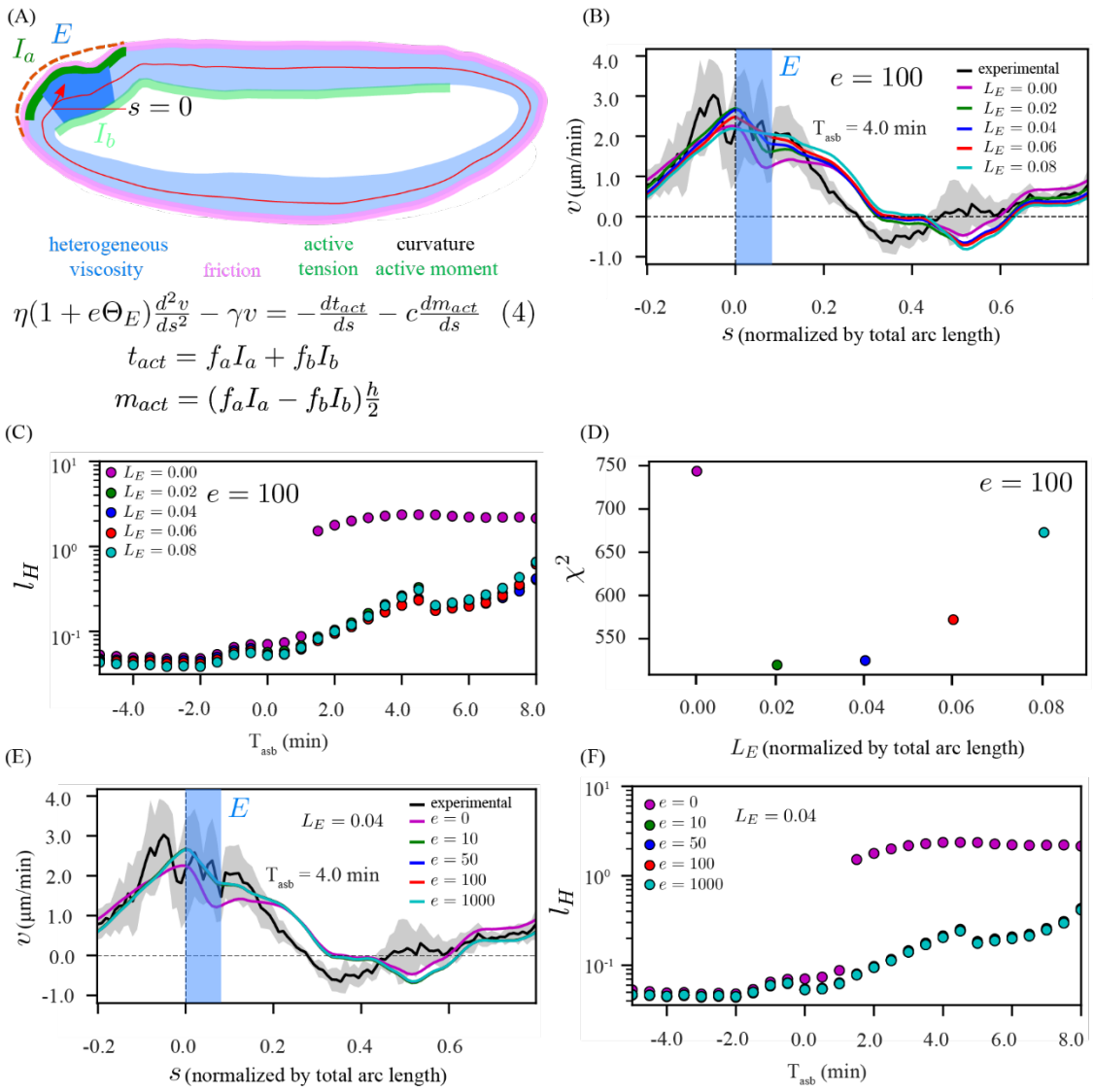

Fig. S7. Curvature-active moment-based model with limited tissue contraction at the region of apical myosin. (A) Schematic representation of our model, equation (4), which is similar to **Fig. 5D** in main text**,** but with an additional domain *E* (dark blue region) where the localized viscosity is increased by a factor *e*. **(B)** Experimentally measured spatial profile of velocity v (black) and result of fits (using procedure described in **Fig. 3** in the main text) of equation (4) with increased value of viscosity fixed at *e* = 100, shown for five values of the length of high viscosity domain L_E (centered around and restricted within the apical myosin domain, and). In fitting, all parameters but the hydrodynamic length (l_H) constant over time. **(C)** Temporal profile of l_H corresponding to fitting described in **B**. **(D)** Comparison of the fit quality for fitting curves in **B**: chi-square values (χ^2), summed over all time points. **(E)** Similar to panel **B** but fitting was done with a fixed value of the length L_E = 0.04 and for five different values of increase in viscosity *e*. **(F)** Temporal profile of l_H corresponding to fitting described in panel **E**. Here, l_H is given in units of epithelial length L~1000 μm. The shaded regions associated to experimental data is the standard deviation, computed over 6 embryos.

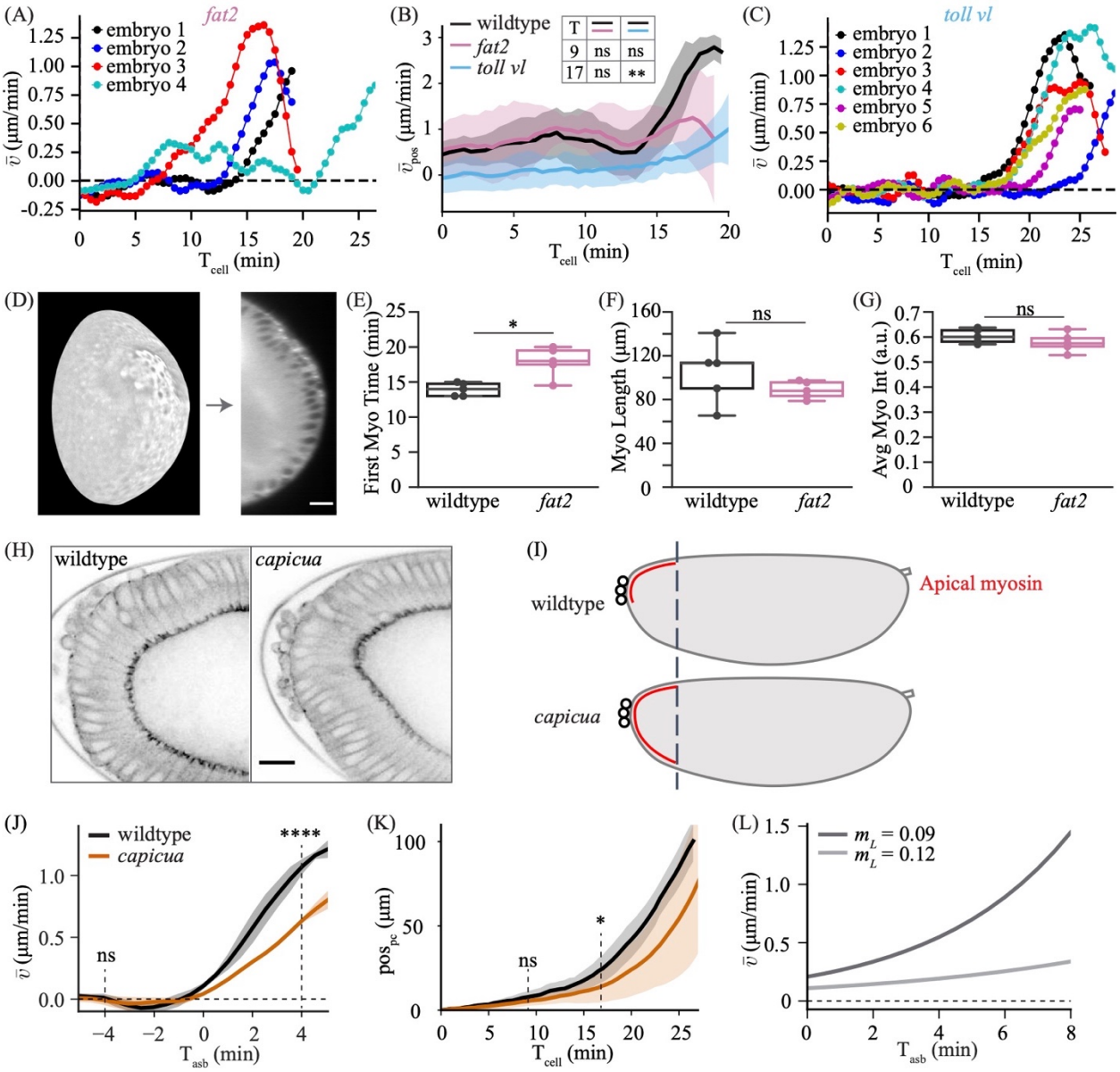

Fig. S8. *fat2* and *capicua* characterization. (A) Temporal profile of $\underline{v}$ for individual *fat2* embryos. **(B)** Temporal profile of posterior averaged velocity $\bar{v}_{pos}$ for wildtype (black), *fat2* (pink), and *toll vl* (blue) embryos. **(C)** Temporal profile of $\bar{v}$ for individual *toll vl* embryos. **(D)** A 3D lightsheet image of a *fat2* embryo and the corresponding 2D cross-section used for data analysis. Scale bar is 20 μm. **(E)** Quantification of the time at which the first puncta of myosin appears (First Myo Time) for 5 wildtype and 5 *fat2* embryos. **(F)** Quantification of the length of the posterior myosin domain (Myo Length) 2.5 minutes after the first large movement of the pole cells for 5 wildtype and 5 *fat2* embryos. **(G)** Quantification of average brightness of the myosin domain 2.5 minutes after the first large movement of the pole cells normalized to the average brightness of the cellularization front 5 minutes after cellularization (Avg Myo Int) for 5 wildtype and 5 *fat2* embryos. **(H)** View of the posterior of a wildtype (left) and *capicua* (right) embryo imaged for *sqh*::GFP.

Scale bar is 20 μm. Note: the *capicua* embryos were imaged with a single copy of s*qh*::GFP and GAP43::mSc. **(I)** Schematic showing the change in apical myosin domain in *capicua* embryos. **(J)** Experimental spatially averaged tangential velocity as a function of time since symmetry breaking for 5 wildtype, and 5 *capicua* embryos. **(K)** Pole cell position (pos_{pc}) as a function of time for 6 wildtype, and 9 *capicua* embryos. **(L)** Average velocity of tissue flow resulting from simulations performed on elliptical embryos with different length of myosin domain (m_L; see ***SI Appendix***). Comparisons in **B**, **E, F**, **G, J** and **K** performed using two-tailed unpaired t-test. ns, not significant; *, $p < 0.05$; **, $p < 0.01$; ****, $p < 0.0001$.

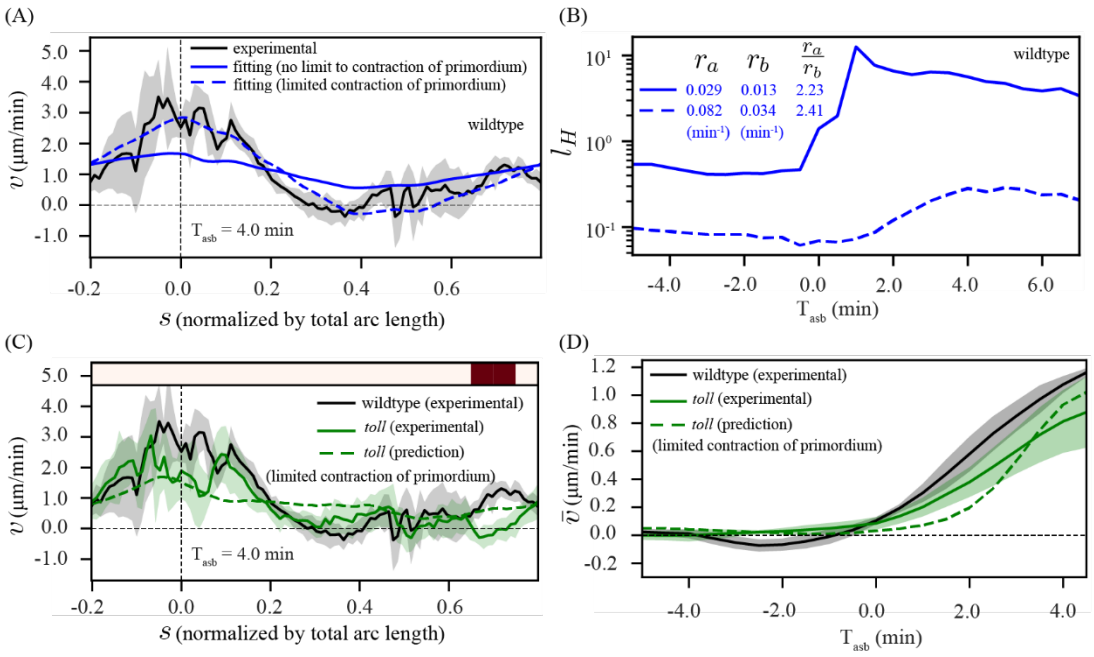

Fig. S9. wildtype, *toll vl*, fitting and prediction. (A) Experimentally measured spatial profile of velocity v (black) in wildtype embryos and result of fits of equation (3) in panel **Fig. 5D** in main text (blue solid curve, no limit to contraction of the primordium) and equation (4) in panel **Fig. S7A** (blue dashed curve, limited contraction of the primordium with e = 100 and L_E = 0.04), representative time T_{asb} = 4 min. The fits were performed using the same procedure as described in **Fig. 5G** (magenta curve in main text). **(B)** Parameters corresponding to fits in panel **A**, temporal profile of the hydrodynamic length l_H (as curves) and other constant parameters r_a, r_b and their ratio (in legend). **(C, D)** Prediction of velocity for *toll vl* using parameters from wildtype in panel **B** (blue dashed line), and myosin and curvature data from *toll vl*. **(C)** Experimentally measured spatial profile of velocity v in wildtype (black) and *toll vl* (green solid curve), and predicted spatial velocity profile for *toll vl* (green dashed curve). Bar on top shows results of a double-tailed Student's t-test (white regions – not significantly different, red regions – significantly different with $p<0.05$). **(D)** Experimentally measured temporal profile of spatially averaged velocity $\bar{v}$ in wildtype (black) and *toll vl* (green solid curve), and predicted temporal profile of spatially averaged velocity for *toll vl* (green dashed curve).

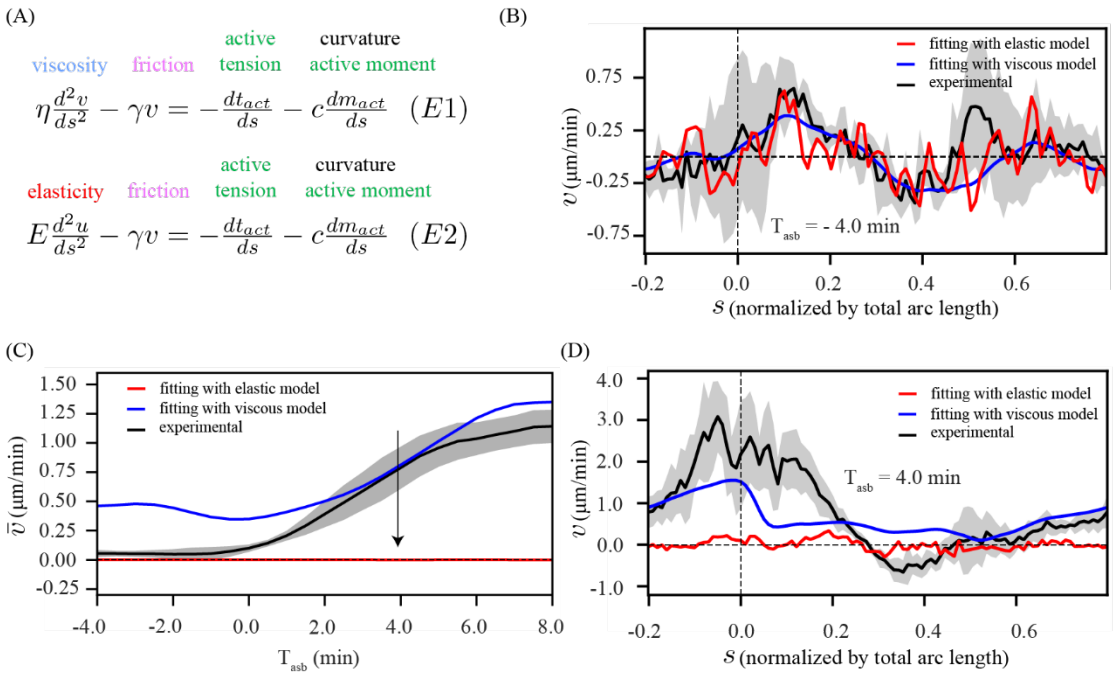

Fig. S10. Comparison of our viscous model with an elastic model. (A) Equations for the viscous model (same as equation 3 in Fig. 5 in the main text or equation S22 in the SI) and the elastic model (same as equation S27 in the SI). **(B)** Symmetric phase: fits of the viscous model (blue, equation E1 without the curvature term) and the elastic model (red, equation E2 without the curvature term) at a representative time point in symmetric phase (T_{asb} **= -**4 min)**.** Both fits were obtained by simultaneously fitting the respective equations to all experimentally measured velocity data (black) between T_{asb} = -4 min and T_{asb} = 0 min, where we kept all parameters constant over time. **(C,D)** Symmetric + asymmetric phase: **(C)** Experimental temporal profile of spatially averaged velocity $\bar{v}$ (black) and average velocity curved obtained from fits to equations E1 (blue) and E2 (red). The fits were obtained by simultaneous fit of the respective equations to the experimentally measured spatio-temporal velocity profiles for time points between T_{asb} = -4 min and T_{asb} = 8 min, where all parameters were kept constant over time. **(D)** Corresponding spatial fit curves at a representative time point during the polarized-flow phase (T_{asb} **=** 4 min)**.** The shaded regions associated to experimental data indicate the standard deviation, computed over 6 ets embryos.

Legends for Movies S1 to S8:

Movie S1 (separate file): Time-lapse of early *Drosophila* morphogenesis in a wildtype embryo. Imaged in the sagittal plane on a two-photon microscope labeled with GAP43::mScarlet (top) and *sqh*::GFP (bottom).

Movie S2 (separate file): Tissue dynamics in wildtype and *ets* embryos. Time-lapse of myosin activation in a wildtype (top) and *eve, twist, snail embryo* (bottom) synchronized with respect to the time when the cellularization front passes the nuclei in the dorsal posterior.

Movie S3 (separate file): Tracking of pole cells in a wildtype embryo. Time-lapse of tissue dynamics in an embryo labeled for cell membrane maker GAP43::mScarlet. The green dot shows the position used to calculate pole cell movement over time (as in **Fig. 1D**).

Movie S4 (separate file): Direction of flow in *toll vl* embryos. Time-lapse of three *toll vl* mutant embryos that flow indifferent directions. The top embryo flows dorsally, the middle embryo flows laterally, and the bottom embryo flows ventrally.

Movie S5 (separate file): Tissue dynamics in wildtype, *toll vl,* and *cta* embryos. Time-lapse of myosin activation in a wildtype (top), *toll vl* (middle), and *cta* (bottom) embryos synchronized with respect to the time when the cellularization front passes the nuclei in the dorsal posterior.

Movie S6 (separate file): Tissue dynamics in wildtype and *scab* knockout embryos. Time-lapse of myosin activation in a wildtype (top) and *scab* knockout (bottom) embryos synchronized with respect to the time when the cellularization front passes the nuclei in the dorsal posterior.

Movie S7 (separate file): Tissue dynamics in wildtype and *fat2* embryos. Time-lapse of myosin activation in a wildtype (top) and *fat2* (bottom) embryos synchronized with respect to the time when the cellularization front passes the nuclei in the dorsal posterior.

Movie S8 (separate file): Tissue dynamics in wildtype and *cic* embryos. Time-lapse of myosin activation in a wildtype (top), and *cic* (bottom) embryos synchronized with respect to the time when the cellularization front passes the nuclei in the dorsal posterior.

SI References

1. G. Salbreux, F. Jülicher, Mechanics of active surfaces. *Phys. Rev. E* **96**, 032404 (2017).
2. K. Bambardekar, R. Clément, O. Blanc, C. Chardès, P.-F. Lenne, Direct laser manipulation reveals the mechanics of cell contacts in vivo. *Proc. Natl. Acad. Sci. U. S. A.* **112**, 1416–1421 (2015).
3. A. D'Angelo, K. Dierkes, C. Carolis, G. Salbreux, J. Solon, In vivo force application reveals a fast tissue softening and external friction increase during early embryogenesis. *Curr. Biol.* **29**, 1564-1571.e6 (2019).
4. A. D. Wessel, M. Gumalla, J. Grosshans, C. F. Schmidt, The mechanical properties of early *Drosophila* embryos measured by high-speed video microrheology. *Biophys. J.* **108**, 1899–1907 (2015).